Check for updates

FULL ARTICLE

Impairments of cerebral blood flow microcirculation in rats brought on by cardiac cessation and respiratory arrest

Gennadii Piavchenko* [1,2,3] | Igor Kozlov[4] | Viktor Dremin[3,4,5] | Dmitry Stavtsev[4,6] | Evgeniya Seryogina[3] | Ksenia Kandurova[4] | Valery Shupletsov[4] | Konstantin Lapin[2] | Alexander Alekseyev[3] | Sergey Kuznetsov[1] | Alexander Bykov[7] | Andrey Dunaev[3,4] | Igor Meglinski* [1,2,5,7]

[1]Histology, Cytology and Embryology Department, I.M. Sechenov First Moscow State Medical University, Moscow, Russia
[2]V.A. Negovsky Scientific Research Institute of General Reanimatology, Federal Research and Clinical Center of Intensive Care Medicine and Rehabilitology, Moscow, Russia
[3]Cell Physiology and Pathology Laboratory, Orel State University, Orel, Russia
[4]R&D Center of Biomedical Photonics, Orel State University, Orel, Russia
[5]College of Engineering and Physical Sciences, Aston University, Birmingham, UK
[6]Institute of Biomedical Systems, National Research University of Electronic Technology, Zelenograd, Moscow, Russia
[7]Faculty of Information and Electrical Engineering, University of Oulu, Oulu, Finland

Correspondence
* Email: gennadii.piavchenko@staff.sechenov.ru and/or i.meglinski@aston.ac.uk

Present Address
8/2 Trubetskaya str., Moscow, 119991, Russia

The impairments of cerebral blood flow microcirculation brought on by cardiac and respiratory arrest were assessed with multi-modal diagnostic facilities, utilising laser speckle contrast imaging, fluorescence spectroscopy and diffuse reflectance spectroscopy. The results of laser speckle contrast imaging show a notable reduction of cerebral blood flow in small and medium size vessels during a few minutes of respiratory arrest, while the same effect was observed in large sinuses and their branches during the circulatory cessation. Concurrently, the redox ratio assessed with fluorescence spectroscopy indicates progressing hypoxia, NADH accumulation and increase of FAD consumption. The results of diffuse reflectance spectra measurements display a more rapid grow of the perfusion of deoxygenated blood in case of circulatory impairment. In addition, consequent histopathological analysis performed by using new tissue staining procedure developed in-house. It shows notably higher reduction of size of the neurons due to their wrinkling within brain tissues influenced by circulation impair. Whereas, the brain tissues altered with the respiratory arrest demonstrate focal perivascular edema and mild hypoxic changes of neuronal morphology. Thus, the study suggest that consequences of a cessation of cerebral blood flow become more dramatic and dangerous compare to respiratory arrest.

KEYWORDS:
cerebral blood flow, cardiac cessation, respiratory arrest, microcirculation, brain imaging, laser speckle contrast

1 | INTRODUCTION

Nowadays, prediction of early damage and microstructural reorganisation of cerebral tissues composition is crucial for numerous acute states, and especially those associated with a risk of brain death. The clinical death is typically caused by cessation of blood circulation and/or respiratory arrest[1]. In current study, we combined use of modern photonics-based modalities, such as laser speckle contrast imaging (LSCI), fluorescence spectroscopy (FS) and diffuse reflectance spectroscopy (DRS), the impairments of cerebral blood flow microcirculation brought by cardiac cessation and respiratory arrest are comparatively investigated.

LSCI is well-known imaging modality[2], and used extensively in a number of blood microcirculation studies, including those of tumour angiogenesis[3], cutaneous vessels reaction to allergens[4,5], skin complication of diabetes [6], respiratory-related blood flow oscillations[7], and visualisation of cerebral

This article has been accepted for publication and undergone full peer review but has not been through the copyediting, typesetting, pagination and proofreading process which may lead to differences between this version and the Version of Record. Please cite this article as doi: 10.1002/jbio.202100216

This article is protected by copyright. All rights reserved.

Accepted Article

vascular network [8]. It has been also demonstrated that with a combined application of LSCI and intravital fluorescence imaging the transcranial visualisation of brain's vascular bed can be performed in terms of blood flow within single arteries and veins[9–11].

DRS is a promising inexpensive non-invasive method that is able to show real-time dynamics of acute cerebral pathologies and to assess cerebral hemodynamics[12]. When FS and DRS are successfully utilised for monitoring metabolic and morphological changes in biological tissues *in vivo*[13].

In addition to the optical methods, histopathology is widely used for quantitative assessment of brain damage and direct visualisation of structural malformations associated with diseases and brain death. Histopathological analysis, used for the pathological changes within brain tissues, includes both routine staining with hemotoxylin and eosin (HE) as well as own new method of staining. In case of classical approach of HE staining, we are able to see only the most expressed pathology, making conclusion questionable. With new method we detect strong neuronal ischemia and vascular disorders as well as two types of neurons stained with cresyl violet and silver impregnation. The neuronal cells vary in structural and tinctorial properties and indicate various types of pathologies.

Thus, LSCI and DRS are used for evaluation of impairments of cerebral blood flow and blood microcirculation brought on by acute hypoxia provoked by respiration arrest and cardiac cessation. The associated variations in metabolic activities in cerebral cortex are assessed quantitatively by FS. In addition, the histopathological analysis is used to detect a hypoxic impact on the cerebral cortex in terms of structural morphological changes in postmortem brain tissues.

2 | MATERIALS AND METHODS

The experimental system combining LSCI, DRS and FS imaging/diagnostic modalities is presented in Figure 1.

The laser source (10 mW, 785 nm operating wavelength, Thorlabs, Inc., USA) illuminates the area of interest through a diffuser. The back-scattered light is collected via the lens (MVL25TM23, Thorlabs, Inc., USA), and the laser speckles analysis is performed by high-resolution CMOS camera (DCC3260M, 1936×1216 pixels and 5.86-pixel size, Thorlabs, Inc., USA). To eliminate single scattering, two crossed polarizers are placed in front of camera objective and laser module (see Fig.1). The speckle contrast is counted for 40 Hz frame rate and 20 ms expose time, as[14]:

$$C = \frac{\sigma}{\langle I \rangle_k}, \tag{1}$$

where σ is the standard deviation for the intensity of the back scattered light, $\langle I \rangle_k$ is the mean intensity value, $\langle ... \rangle$ denotes averaging by k values of the sequential stacks of images ($k = 40$). The spatial averaging of raw speckle image obtained with CMOS camera is performed utilising 5×5 pixels sliding window[10]. This approach aims to improve the signal-to-noise ratio and image quality. Speckle perfusion index (SFI) is defined as[15]:

$$SFI = \frac{1}{2TC^2}, \tag{2}$$

where T is the exposure time of camera.

Every frame of stack is normalized by frame with the lowest mean of SFI. Thus, relative SFI is calculated as:

$$relative\ SFI = 100 \times \frac{SFI(t)}{baseline\ SFI}, \tag{3}$$

where $baseline\ SFI$ is the averaged map by first 30 frames.

LSCI measurements are recorded at the same time with FS and DRS measurements[13]. The FS mode includes 365 nm LED and 450 nm laser diode to excite the fluorescence of NADH and FAD coenzymes[16,17]. Optical filters are used with cut off wavelengths of 400 and 490 nm (Thorlabs Inc., USA), respectively, to attenuate the backscattered light. DRS mode includes 360 to 2400 nm tungsten halogen light source HL-2000-FHSA (Ocean Insight, USA). The FS and DRS spectra are recorded by "FLAME" spectrometer (Ocean Insight, USA) and analyzed in the range of 400 to 900 nm. The custom application is developed in MATLAB (MathWorks, Inc., USA) environment for data recording, saving and controlling the setup.

The computational analysis of spatial localisation of the LSCI and FS detected signals[18,19] at 785 nm shows that the effective penetration depth in rodents tissues lies in a range $\sim\ 0.5 - 0.7\ mm$). Since the thickness of skin and skull in rodents is about $\sim 0.5\ mm$, the young rats have been selected for non-invasive transcranial cerebral imaging.

To deliver the optical radiation into the cortex, a custom fibre-optic probe is applied (see Fig.1). The probe has 1 mm diameter and 20° bevel to ensure a good contact as well as not to damage brain tissues significantly. The probe contains 10 optical fibres (0.22 NA). The central one (200 μm in diameter) the light from the tissue surface to the spectrometer[17], whereas the surrounding fibres (100 μm in diameter, 3 fibres per light source). To avoid uncertainties in spectral measurements associated with the local suppression of superficial soft tissues[20,21] the probe is placed close to the skin surface without touching it. The FS and DRS spectra are recorded during 1.5 seconds and 0.5 seconds, respectively. To avoid a photobleaching effect, fluorescence excitation sources have been turned off between the measurements. The examples of registered raw speckle image, FS and DRS are shown in Figure 1b,c,d. Both two weeks old and two months old male Wistar rats were used in the experiments. All animals were kept in controlled environmental conditions ($20 - 26°C$ of temperature, $50 - 60\%$ of humidity, 12 hours day-night cycle and 10

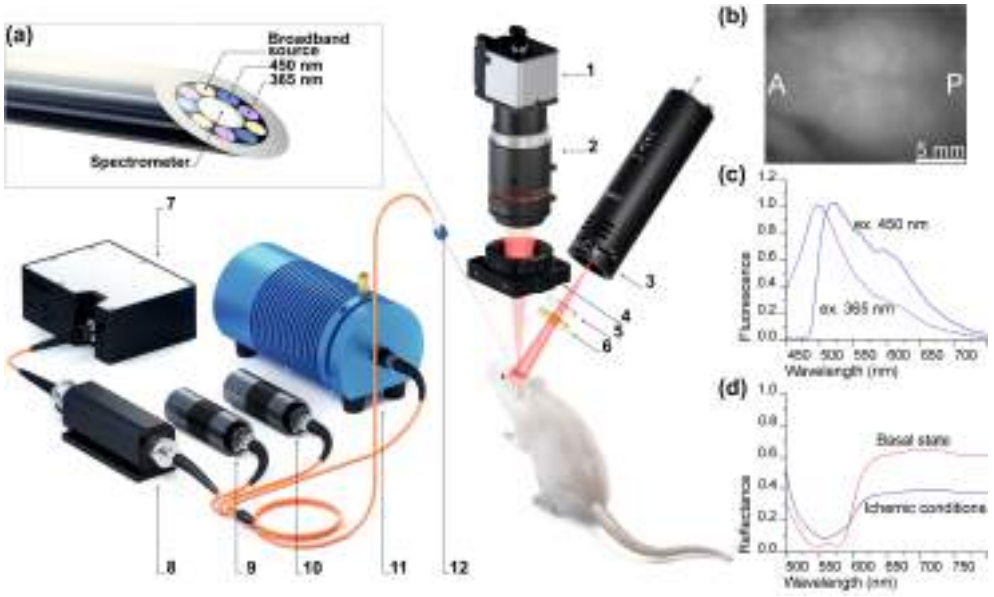

FIGURE 1 Experimental multi-modal imaging system developed in-house (a): 1 – CMOS camera, 2 – camera lens, 3 – 785 *nm* laser, 4, 5 – polarisers, 6 – diffuser, 7 – spectrometer, 8 – filter holder, 9 – 365 *nm* LED, 10 – 450 *nm* laser diode, 11 – halogen lamp, 12 – needle probe; close-up look of the needle probe. Example of raw speckle image from rat brain surface (b), "A" denotes "anterior" and "P" denotes "posterior" anatomical directions; registered fluorescence (c) and diffuse reflectance spectra (d);

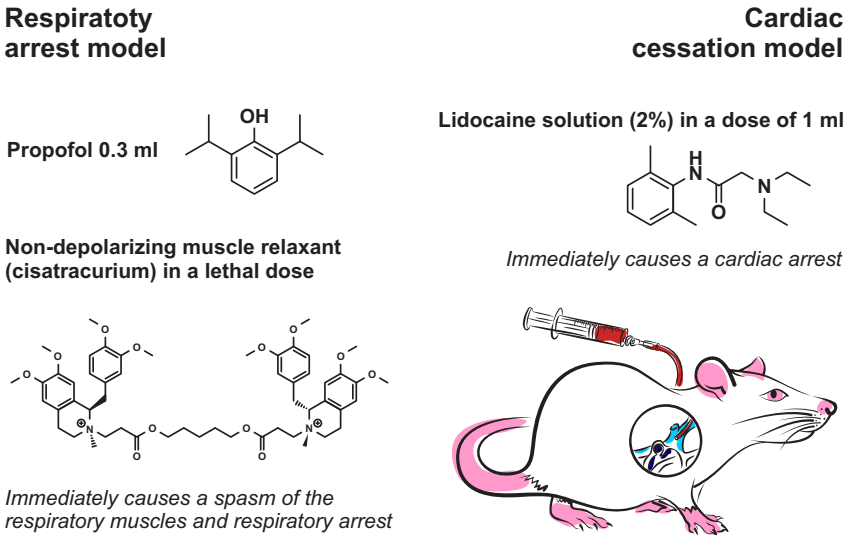

FIGURE 2 Schematic presentation of respiratory and cardiac cessation. After placement in the stereotaxic apparatus the animal was administrated with drugs that caused immediate respiratory arrest (propofol followed by cisatracurium) or acute cardiac cessation (lidocaine solution).

times air exchange per hour) in accordance with the principles of Good Laboratory Practice[22].

The animals were anaesthetized by an intramuscular injection of Zoletil drug (dose – 25 mg/kg, Vibrac, France) and catheterized into right external jugular vein with PM-60 polymer catheter (SciCat, Russia, $d_{ext} = 0.8\ mm$, $d_{int} = 0.4\ mm$). The jugular veins catheterization approach is anatomically easily accessible with a minimal influence on the circulatory system, and is also accompanied by a lower risk of blood loss. The injection of drug into the jugular vein in comparison with the tail vein provides better compatibility[23]. After the anesthesia, the animal is placed on a heating table to control body temperature and is fixed in a 3D-printed animal body holder, developed in-house, to avoid movement artefacts[24].

Accepted Article

Accepted Article

All the manipulations with the animals are approved by the ethical committee of the Orel State University named after I.S. Turgenev (protocol No. 10, October 16, 2018).

The experimental models of respiratory and cardiac arrest are performed for the corresponding animals groups by the injection of drugs combination via catheter (Fig.2). We have checked the heart rate (to confirm the cardiac cessation) with an electrode detecting the heart beats during the experiment. We also counted the respiratory rate (number of diaphragm contractions) by a visual registration of breathing acts. As far as cisatracurium immediately causes a respiratory muscles spasm, any last diaphragm contraction has been considered as a breathing stop in the animal.

After LSCI, FS, DRS imaging and spectra recording, brains of all the animals were fixed in buffered formalin. Paraffin embedded sections of 5 μm thickness are prepared with Microm HM 450 microtome (Microm International GmbH, Germany) and stained with HE by standard protocols[25] and with our own patented Nissl staining and silver impregnation combined method[26]. This new approach allows to see both silver impregnated and cresyl violet stained neurons with different structural and functional properties. The prepared slides were studied with Leica DM4 M Microscope (Leica Microsystems GmbH, Germany) focusing on finding the possible ischemia and vascular pathology changes in the motor cortex area, as this region mostly contributes in the motor behavior regulation (functioning as motor-related areas of cortex[27]). Paxinos and Watson Rat Brain Stereotaxic Atlas[28] is used as a reference guideline.

3 | RESULTS AND DISCUSSION

The impairments of cerebral blood flow microcirculation in cardiac cessation and respiratory arrest are presented in Figure 3. Anatomical direction signs are same as Fig. 1(b). The cerebral blood flow microcirculation measured with LSCI at normal conditions are seen in Fig.3-a and Fig.3-d. Fig.3-b and Fig.3-e show the map of cerebral blood flow microcirculation after 1 minute of respiratory arrest and cardiac cessation, respectively, whereas Fig.3-c and Fig.3-f represent same mappings after 2 minutes passed.

Temporal variations of relative SFI observed for the areas which correspond to the large (venous sinus, $\sim$ 100 μm in diameter), medium (veins of medium calibre, $\sim 30-40$ μm in diameter) and small (vessels of microcirculation, $\sim 2-10$ μm in diameter) cerebral blood vessels (Fig.4-a, 4-b) are presented in Figure 4-c,d,e. As one can see, the relative SFI becomes steady for the first 30 seconds of measurements for both models. While, for the respiration arrest it takes 1 minute ($0.5-1.5$ min) to get an extensive decrease of the relative SFI while in case of cardiac cessation it occurs in few seconds (see Fig.4). Further, a monotonic decrease of the relative SFI is observed with a flop between 6 and 8 minutes of observation. The obtained results suggest that for the respiration arrest the blood flow becomes most influenced first in medium and large size vessels (see Fig.4-c and Fig.4-e, respectively), with the following monotonic decrease of flow. Whereas in small vessels the intensity of blood microcirculation decreasing after first minute is preserved both in case of respiratory arrest and cardiac cessation (see Fig.4-d). The blood flow in the venous sinus is dropped significantly and much faster in case of cardiac cessation (see Fig.4-e).

The results of FS and DRS measurements analysed with Origin Pro (OriginLab Corp., USA) and MATLAB, are presented in Figure 5. In the FS measurements, the maxima of emission intensity at 490 to 510 nm (for the excitation wavelength of 365 nm) and 510 to 530 nm (for 450 nm), respectively, are caused by the dominant contribution of NADH (IF_{NADH}) and FAD (IF_{FAD}). The redox ratio (RR)[29] defined as[30,31]:

$$RR = \frac{IF_{NADH}}{IF_{FAD}} \tag{4}$$

is used to evaluate a metabolic changes of brain tissues associated with the impairments of cerebral blood flow microcirculation brought by cardiac cessation and respiratory arrest.

The RR demonstrates a progressive increase in hypoxia, an accumulation of NADH and increased FAD consumption. Trends identification for the full duration of the experiment is carried out using an exponential fitting with a R-square evaluation. These results are well agreed with the results of an alternative study[32,33]. The changes of RR are more expressed for the case of respiration arrest, and showing less influence in the acute cerebral cortex ischemia due to cardiac cessation. The acute intensity changes are observed for the first 5 minutes after the heart arrest. The increase of RR is caused by growth of NADH-associated fluorescence and decrease of FAD. The obtained result suggests that blood circulation fail leads to a more acute progression of ischemia and to following metabolic derangements in brain cortex.

The DRS measurements at the range of wavelengths associated with oxy- (540 nm) and deoxy- (560 nm) absorption peaks of hemoglobin, as well as at the isobestic point of 805 nm of oxy- and doxy- absorption provides an extra opportunity to assess the changes in blood content[34]. The results of DRS measurements show relatively steady dynamics of the reflectance ratio between maximum and minimum values, that do not exceed 5% (see Fig.5-b). Both cases demonstrate reflectance changes (see Fig.5-c and Fig.5-d) that are associated with the decrements of oxyhemoglobin within the sampling volume. These changes have no significant impact on the results of FS which are influenced by metabolic changes due to hypoxia[35,36].

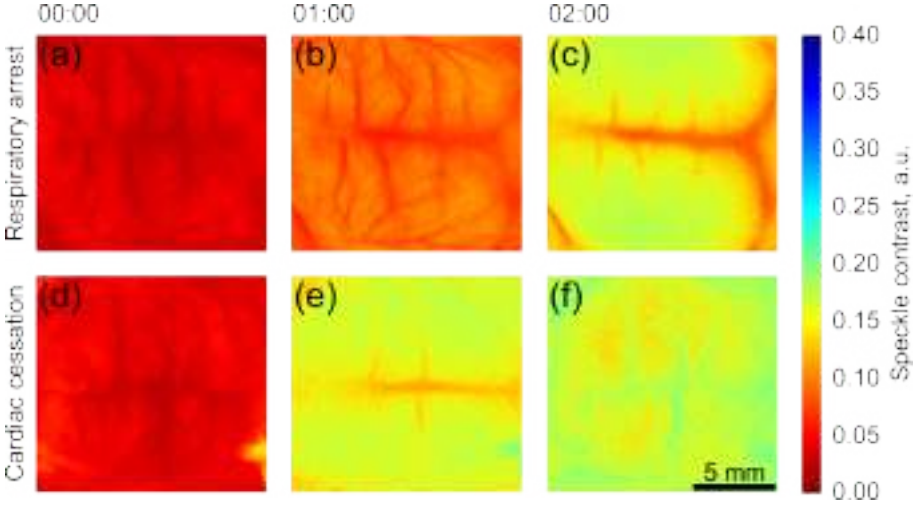

FIGURE 3 Blood flow dynamics in time. The upper row corresponds to respiration impair, and the lower one corresponds to cardiac cessation. Notable changes appear from 1st minute of the recording (b, e). Video for blood flow dynamics is available (Rat brain. Cardiac cessation and respiratory arrest, 191,4 Mb, .avi [URL: https://doi.org/10.5281/zenodo.4739049])

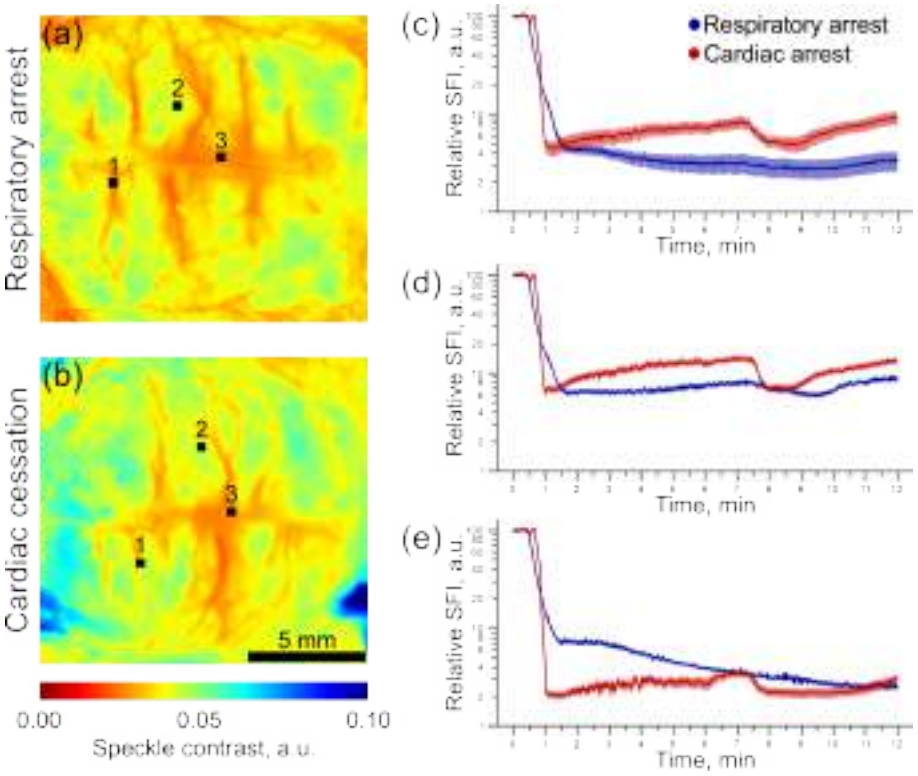

FIGURE 4 The LSCI images observed during respiratory arrest (a) and cardiac cessation (b) arrest with the selected areas of particular groups of vessels: 1 – veins of medium calibre, 2 – vessels of microcirculation, 3 – venous sinus. Corresponded temporal variations of relative SFI (c, d, e) observed during respiratory (blue) and cardiac (red) arrest in the selected areas: 1, 2, 3. Anatomical direction signs are same as Fig. 1(b).

In addition to the results of LSCI, FS and DRS measurements mentioned above, the histopathology analysis of brain tissues is presented in Figure 6. In the brain cortex sections of the first respiration arrest group a focal perivascular edema and mild hypoxic changes of neuronal morphology are clearly seen (see Fig.6-a). In the case of cardiac cessation, the brain cortex

Accepted Article

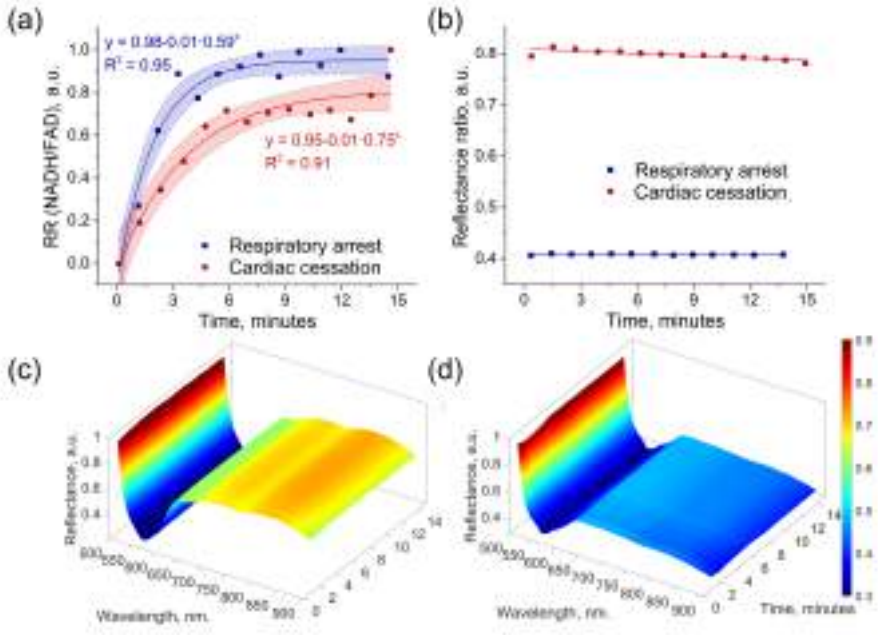

FIGURE 5 The results of FS and DRS measurements: (a) redox ratios of fluorescence intensity (maxima associated with NADH and FAD); (b) DRS ratio obtained at 540 and 805 *nm* during respiration arrest (c) and cardiac cessation (d).

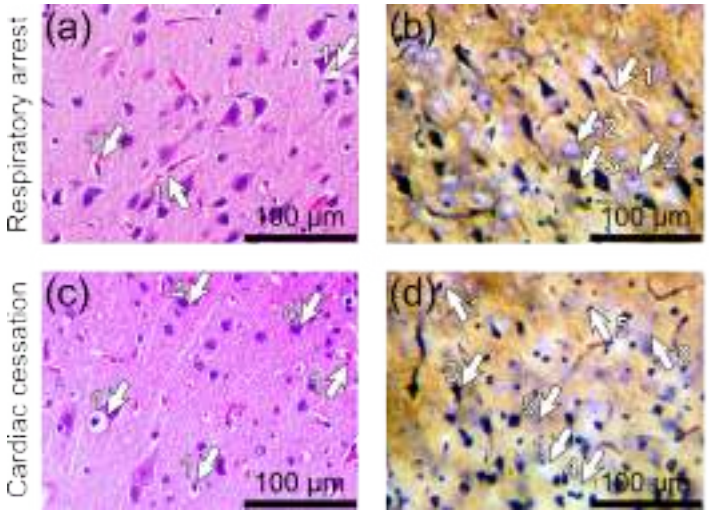

FIGURE 6 The results of histopathological analysis of coronal brain tissue sections *in vitro*: (a, c) rat motor cortex stained with hematoxylin and eosin; (b, d) rat motor cortex stained with method developed in-house utilising cresyl violet and silver impregnation combination. The circles highlight vessels with perivascular edema (1), cresyl violet stained neurons with nucleoli (2), totally impregnated neurons (3), necrobiotic cells (4), ghost-like cells (5).

contains a significant number of hyperchromic wrinkled neurons, glial nodules at the site of necrotic neurons, as well as pericellular edema in all tissue sections (see Fig.6-c).

For specimens stained with the new approach developed in-house, in both cases the pathological changes in nervous tissue morphology are observed (see Fig.6-b and Fig.6-d). The results of histopathology analysis for the group of animals with cardiac cessation also show a more considerable size reduction of impregnated and cresyl violet stained neurons due to their wrinkling. There are also initial stages of anucleated pale "ghost-like" neurons forming, a less distinct neuropil structure, a decreased basophilia of cellular cytoplasm (due to the reduction of activity in synthetic apparatus, or chromatophilic substance), a less smoothed outline of the neurons as well as

Accepted Article

dark impregnated neurons, (see Fig.6-b, and Fig.6-d). The new staining approach allows to compare the changes in neuronal morphology provoked by impairments of cerebral blood flow microcirculation brought by cardiac cessation and respiratory arrest.

4 | SUMMARY AND CONCLUSIONS

In acute respiratory arrest there is a gradual increase of hypoxia as well as a slowdown of hemodynamics. For acute circulatory impair we observe an immediate cease of oxygenated blood supply to the brain cortex. We conclude that acute cardiovascular impair (e.g., sudden cardiac arrest) is more life-threatening and leads to a faster increase of neuronal metabolism deficiency in comparison with acute respiratory impair. After long time hypoxia, the biochemical processes shift to the low energy mode and provide a resistance to hypoxia until a state of full anoxia is achieved. The obtained results are well agreed with known literature data. Changes of FS intensities, which lead to a RR increase, might be noticed after 5 minutes, while the trend for DRS ratios remains almost the same, especially in the case of respiration impair. Blood circulation in vessels of cerebral cortex stops in case of respiratory arrest after about 2 minutes while in heart arrest it happens after about 1 minute. Changes in the brain tissue oxygen saturation for heart arrest become evident during the first 5 minutes, but for acute breathing fail there are almost no changes. Heart arrest manifests by a more acute hypoxic state in cerebral cortex comparing to what is happening when breathing is impaired. So, acute cardiovascular impair is more life-threatening. It causes a rapid increase in neuronal metabolic deficiency comparing to acute respiratory impair. This may serve to personalize the management of patients after acute circulatory and respiratory arrest for prognosis and rehabilitation. The utilised multi-modal photonics-based approach of brain tissue functional monitoring may allow to bring a complex assessment with laser speckle and spectroscopy methods for evaluation of brain metabolism changes in neurosurgical patients.

ACKNOWLEDGMENTS

The authors disclose receipt of financial support for the research, authorship, and/or publication of this article as following: G.P. and S.K. acknowledge the support from the Ministry of Science and Higher Education of the Russian Federation withing the framework of State support for the creation and development of World-Class research Centres “Digital Biodesign and Personalized Healthcare” No 075-15-2020-926. V.D. kindly acknowledges personal support from the European Union’s Horizon 2020 research and innovation program under the Marie Skłodowska-Curie grant agreement No. 839888. A.D. and I.M. acknowledge funding from the Academy of Finland (grant No. 326204). This work has been also partially supported by the European Union’s Horizon 2020 research and innovation programme under grant agreement No.863214 - NEUROPA project.

CONFLICT OF INTEREST

The authors declare no potential conflict of interests.

References

[1] A. Walker, *Cerebral Death*, 3rd edition., Baltimore, MD: Urban & Schwarzenberg, **1985**.

[2] W. Heeman, W. Steenbergen, G. van Dam, E. C. Boerma, *J. Biomed. Opt.* **2019**, *24* (8), 080901.

[3] V. Kalchenko, N. Madar-Balakirski, I. Meglinski, A. Harmelin, *J. Biophotonics* **2011**, *4* (9), 645–649.

[4] V. Kalchenko, Yu. Kuznetsov, D. Preise, I. Meglinski, A. Harmelin, *J. Biomed. Opt.* **2014**, *19* (6), 060502.

[5] V. Kalchenko, I. Meglinski, A. Sdobnov, Yu. Kuznetsov, A. Harmelin, *J. Biomed. Opt.* **2019**, *24* (6), 060501.

[6] E. Zharkikh, V. Dremin, E. Zherebtsov, A. Dunaev, I. Meglinski, *J. Biophoton.* **2020**, *13* (10), e202000203.

[7] I. Mizeva, E. Zharkikh, V. Dremin, E. Zherebtsov, I. Makovik, E. Potapova, A. Dunaev, *Microvasc. Res.* **2018**, *120*, 13–20.

[8] V. Kalchenko, D. Israeli, Yu. Kuznetsov, A. Harmelin, *Sci. Rep.* **2014**, *4* (1), 5839.

[9] V. Kalchenko, D. Israeli, Yu. Kuznetsov, I. Meglinski, A. Harmelin, *J. Biophoton.* **2015**, *8* (11-12), 897–901.

[10] V. Kalchenko, A. Sdobnov, I. Meglinski, Yu. Kuznetsov, G. Molodij, A. Harmelin, *Photonics* **2019**, *6* (3), 80.

[11] G. Molodij, A. Sdobnov, Yu. Kuznetsov, A. Harmelin, I. Meglinski, V. Kalchenko, *Phys. Med. Biol.* **2020**, *65* (7), 075007.

[12] R. M. Forti, M. Katsurayama, J. Menko, L. Valler, A. Quiroga, A. L E Falcão, L. M. Li, R. C. Mesquita, *Front. Med.* **2020**, *7*, 147.

[13] V. Dremin, E. Potapova, E. Zherebtsov, K. Kandaurova, V. Shupletsov, A. Alekseyev, A. Mamoshin, A. Dunaev, *Sci. Rep.* **2020**, *10*, 14200.

Accepted Article

[14] J. D. Briers, S. Webster, *J. Biomed. Opt.* **1996**, *1* (2), 174–180.

[15] C. Crouzet, R. H. Wilson, A. Bazrafkan, M. H. Farahabadi, D. Lee, J. Alcocer, B. J Tromberg, B. Choi, Y. Akbari, *Biomed. Opt. Express* **2016**, *7* (11), 4660–4673.

[16] A. C. Croce, G. Bottiroli, *European journal of histochemistry : EJH* **2014**, *58* (4), 2461.

[17] A. V. Dunaev, V. V. Dremin, E. A. Zherebtsov, I. E. Rafailov, K. S. Litvinova, S. G. Palmer, N. A. Stewart, S. G. Sokolovski, E. U. Rafailov, *Med. Eng. Phys.* **2015**, *37* (6), 574–583.

[18] Yu. L. Kuznetsov, V. V. Kalchenko, N. G. Astaf'eva, I. V. Meglinski, *Quantum. Electron.* **2014**, *44* (8), 713–718.

[19] V. Dremin, E. Zherebtsov, A. Bykov, A. Popov, A. Doronin, I. Meglinski, *Appl. Opt.* **2019**, *58* (34), 9398–9405.

[20] A. Popov, A. Bykov, I. Meglinski, *J. Biomed. Opt.* **2017**, *22* (11), 110504.

[21] I. Mizeeva, E. Potapova, V. Dremin, E.A. Zherebtsov, M.A. Mezentsev, V.V Shuleptsov, A. Dunaev, *Clin. Hemorheol. Microcirc.* **2019**, *72* (3), 259–267.

[22] *OECD series on principles of good laboratory practice and compliance monitoring*. https://www.oecd.org/officialdocuments/publicdisplaydocumentpdf/?cote=env/mc/chem%2898%2917&doclanguage=en.

[23] K. V. Thrivikraman, R. L. Huot, P. M. Plotsky, *Brain Res. Brain Res. Protoc.* **2002**, *10* (2), 84–94.

[24] I. M. Gryadunov, G. A. Piavchenko, I. O. Kozlov, E. S. Seryogina, S. L. Kuznetsov, RU patent 200025U1 (10 January 2020).

[25] G. A. P'yavchenko, L. I. Shmarkova, V. I. Nozdrin, *Neurosci. Behav. Physiol.* **2016**, *46* (3), 270–273.

[26] G. A. Piavchenko, D. Pranab, N. S. Novikova, V. I. Nozdrin, RU patent 2666256C2 (6 September 2018).

[27] X. Li, M. A Krol, S. Jahani, D. A. Boas, Helen Tager-Flusberg, M. A. Yücel, *Sci. Rep.* **2020**, *10* (1), 10965.

[28] G. Paxinos, C. Watson, *The rat brain in stereotaxic coordinates: hard cover edition*, Elsevier, **2006**.

[29] B. Chance, B. Schoener, R. Oshino, F. Itshak, Y. Nakase, *J. Biol. Chem.* **1979**, *254* (11), 4764–4771.

[30] J. H. Ostrander, C. M. McMahon, S. Lem, S. R. Millon, J. Q. Brown, V. L. Seewaldt, N. Ramanujam, *Cancer Res.* **2010**, *70* (11), 4759–4766.

[31] K. Staniszewski, S. H. Audi, R. Sepehr, E. R. Jacobs, M. Ranji, *Ann. Biomed. Eng.* **2013**, *41* (4), 827–836.

[32] V. Shupletsov, K. Kandurova, E. Seryogina, G. Piavchenko, V. Dremin, A. Mamoshin, A. Dunaev, *Proc. SPIE* **2019**.

[33] V. Dremin, E. Potapova, A. Mamoshin, A. Dunaev, E. Rafailov, *Laser Phys. Lett.* **2020**, *17* (11), 115605.

[34] B.C. Wilson, S.L. Jacques, *IEEE Journal of Quantum Electronics* **1990**, *26* (12), 2186–2199.

[35] A. I. Zherebtsova, V.V. Dremin, I. N. Makovik, E. A. Zherebtsov, A. V. Dunaev, A. Goltsov, S. G. Sokolovski, E. U. Rafailov, *Frontiers in Physiology* **2019**, *10*, 416.

[36] V. V. Dremin, E. A. Zherebtsov, V. V. Sidorov, A.I. Krupatkin, I. N. Makovik, A. I. Zherebtsova, E. V. Zharkikh, E. V. Potapova, A. V. Dunaev, A. A. Doronin, A. V. Bykov, I. E. Rafailov, K. S. Litvinova, S. G. Sokolovski, E. U. Rafailov, *J. Biomed. Opt.* **2017**, *22* (8), 1–10.

GRAPHICAL ABSTRACT

After an impair of blood and respiration functions there are significantly different changes in the structure and function of brain tissue that we present in this article.

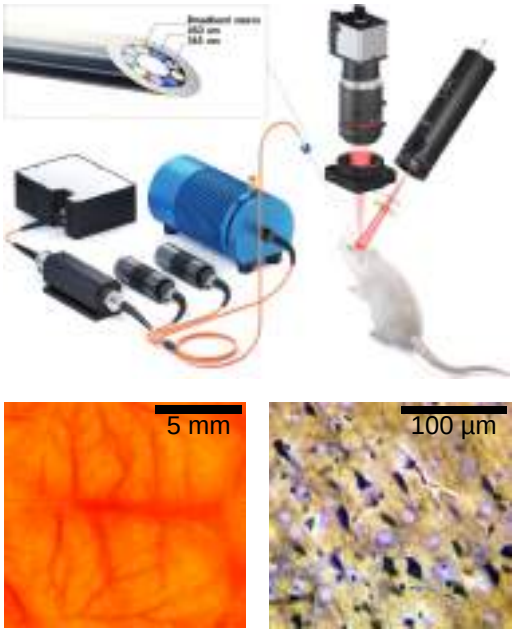

Accepted Article

How to cite this article: G. Piavchenko, I. Kozlov, V. Dremin, D. Stavtsev, E. Seryogina, K. Kandurova, V. Shupletsov, K. Lapin, A. Alekseyev, S. Kuznetsov, A. Bykov, A. Dunaev and I. Meglinski (2021), Impairments of cerebral blood flow microcirculation in rats brought on by cardiac cessation and respiratory arrest, *J. Biophotonics*, *20XX;XX:X*.

Accepted Article